Integrated Devices for Terabit per Second 1.3 and 1.5 Micron WDM/TDM Network Applications

Final Report
June 1, 1996 – September 30, 2001

PI: Prem Kumar, Professor
Department of Electrical and Computer Engineering
Northwestern University, Evanston, IL 60208-3118
Tel: (847) 491-4128; Fax: (847) 491-4455; E-mail: kumarp@northwestern.edu

Co-PI's:
Seng-Tiong Ho, Associate Professor
Department of Electrical and Computer Engineering
and
Bruce W. Wessels, Professor
Departments of Materials Science and Engineering and Electrical and Computer Engineering

20051013 180

Integrated Devices for Terabit per Second 1.3 and 1.5 Micron WDM/TDM Network Applications

Final Report
June 1, 1996 – September 30, 2001

PI: Prem Kumar, Professor
Department of Electrical and Computer Engineering
Northwestern University, Evanston, IL 60208-3118
Tel: (847) 491-4128; Fax: (847) 491-4455; E-mail: kumarp@northwestern.edu

Introduction

A widespread deployment of all-optical networks is expected over the next decade. It is anticipated that the local-area network (LAN) and metropolitan-area network (MAN) speeds will approach 100 Gb/s. Since such LANs and MANs will serve heterogeneous environments, both wavelength-division multiplexed (WDM) and time-division multiplexed (TDM) network architectures are likely to be deployed. To make such networks a practical reality, electro-optical and all-optical devices that operate at speeds in excess of 100 Gb/s and that are compatible with the emerging WDM/TDM architectures will be needed. In addition, for successful commercial deployment, all such devices must be of low cost, which can only be accomplished through integration. Hence, there is an urgent need for developing integrated devices including transmitters, modulators, multiplexers, demultiplexers, amplifiers, etc., that will become the building blocks of the LANs and MANs of the future.

With the above scenario in mind, in June of 1996 a multidisciplinary research program was started at Northwestern University to develop and demonstrate novel, compact, integrated, opto-electronic and optical devices for use in ultrahigh-speed WDM and TDM networks.

Specifically, the multidisciplinary university research initiative at Northwestern had the following program goals:

1. Develop epitaxially grown undoped and doped (Er, Yb) ferroelectric thin films for waveguide-based modulators and other nonlinear-optical applications.

2. Develop semiconductor-based micro-resonator technology for wideband-tunable modulators, multiplexers, and demultiplexers that is capable of high integration density.

3. Demonstrate TDM network applications of fiber-optic parametric nonlinearities using potentially low-cost, high power fiber lasers having wavelength selectivity.

In the following, we present our technical accomplishments during this project. For the sake of presenting the most important results, emphasis in this report is placed on accomplishments during the final two years of the project.

1 Optically active ferroelectric thin films for waveguides and fast electro-optic modulators

The development of highly integrated microphotonic systems that generate, guide, modulate, amplify and detect light would dramatically enhance the capabilities of optical communication systems, local area networks, and chip-to-chip optical interconnects. High index-contrast thin film structures using ferroelectric oxides as the non-linear media have been proposed [1–8].

The program objectives for this part of the research included:

- Synthesis of epitaxial ferroelectric thin films by metalorganic vapor phase epitaxy (MOVPE).
- Development of thin film ferroelectric electro-optic modulators.
- Development of Er-doped thin film optical amplifiers.
- Integration of epitaxial ferroelectric waveguide structures on silicon using metalorganic molecular beam epitaxy (MOMBE).

Accomplishments:

1.1 The synthesis of epitaxial ferroelectric thin films by metalorganic vapor phase epitaxy (MOVPE)

Research centered on the study of deposition parameters for the epitaxial growth of $BaTiO_3$ for waveguides. Both rare-earth doped and undoped films were deposited. Efforts were directed at improving process reproducibility in order to obtain films with uniform thickness, low optical loss, bulk like electro-optic coefficients and improved luminescent efficiency. The role of residual stress in the thin films on non-linear optical properties was studied.
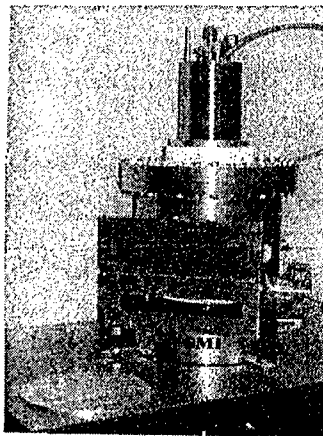

Figure 1   Low pressure MOCVD reactor.

Through process optimization, $BaTiO_3$ films with electro-optic coefficients as high as 260pm/V were prepared. This is the highest EO coefficient reported for $BaTiO_3$ films to date. This shows that that MOVPE is a viable technique for the deposition of high quality non-linear optical materials.

Based on our BaTiO₃ thin film studies, we applied for and received a DURIP grant to obtain an MOVPE reactor so that epitaxial ferroelectric films on four-inch wafers can be deposited. This capability is needed so that high-density integrated optical circuits can be prepared. We are currently working with the vendor, Structure Materials Inc., to design and implement a low pressure, rotating-susceptor, vertical reactor. The reactor will enable the deposition of highly, uniform epitaxial ferroelectrics suitable for integrated optical circuits. We believe that this reactor will be the only one worldwide with capability of depositing large area epitaxial films of ferroelectrics. The delivery date is scheduled for January 2001. Figure 1 shows a prototype of the epitaxial reactor.

1.2 Development of thin film ferroelectric electro-optic modulators

Thin film electro-optic modulators using ferroelectrics as the non-linear optical media were studied. The research involved the study of i) the material factors that determine the electro-optic coefficient and ii) the fabrication and testing of thin film electro-optic modulators. Three ferroelectric materials were examined: $KNbO_3$, $KNbTaO_3$, and $BaTiO_3$.

The transverse electro-optic coefficients and their dynamic response of the thin films were measured using a system previously described. The effect of a bias field on the EO properties of the films was examined. Bias fields up to 4MV/m have been observed to increase the EO response dramatically. For $BaTiO_3$ EO coefficients up to 210pm/V have been measured with the bias field. Figure 2(Left) shows the dynamic response. Upon removal of the bias field, the EO effect slowly returns to its unpoled state. Upon applying a bias field, the EO effect shows hysteresis as shown in Figure 2(Right) similar to that observed for polarization vs. voltage. This observation suggests the removal of anti-parallel domains is the mechanism responsible for the increase in the EO effect upon poling.
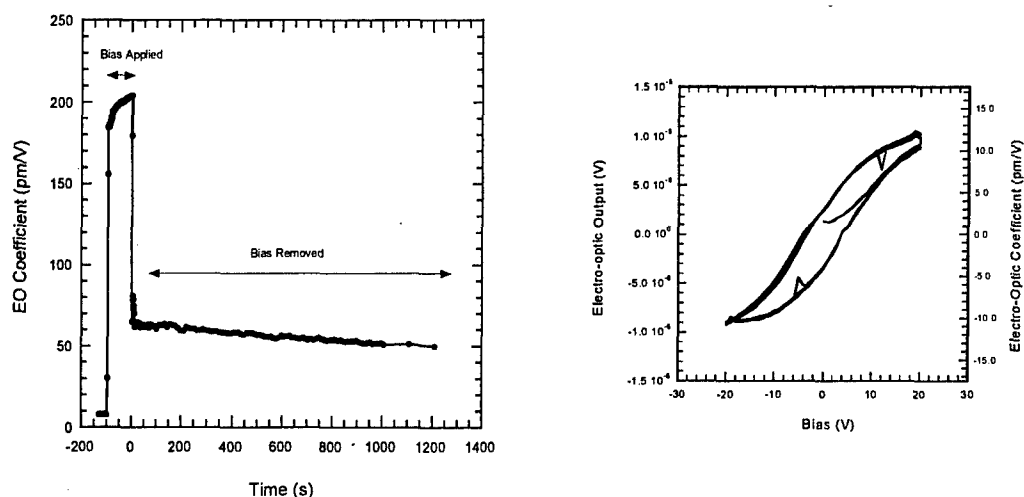

Figure 2   Left – Dynamic response of the EO effect. Right – EO coefficient plotted vs. bias.

To optimize the EO modulator response the directional dependence of the EO effect in the $BaTiO_3$ films was investigated. The EO coefficients were measured for a single film with the E field oriented along and between <100> and <110> directions of the MgO substrate. For these a-

axis oriented $BaTiO_3$ films, the largest EO effect can be produced by applying the electric field at an angle of 45° to the cubic axes (along the <110> zone axis) of the substrate and film [Figure 3(Left)]. The effect of poling by applying a DC bias was also more pronounced in this direction. Modeling of the EO properties of these multiple-domain thin films suggests that this geometry allows access to the large r_{42} EO coefficient. In bulk $BaTiO_3$ this coefficient is ~1300pm/V. Through poling of the films and application of the electric field along <100> effective EO coefficients as high as $r_{42}/\sqrt{2}$ ~920pm/V should be achieved. However, the largest EO effect observed in the $BaTiO_3$ films under these conditions was 260pm/V. The factors limiting the EO properties are the subject of further study.
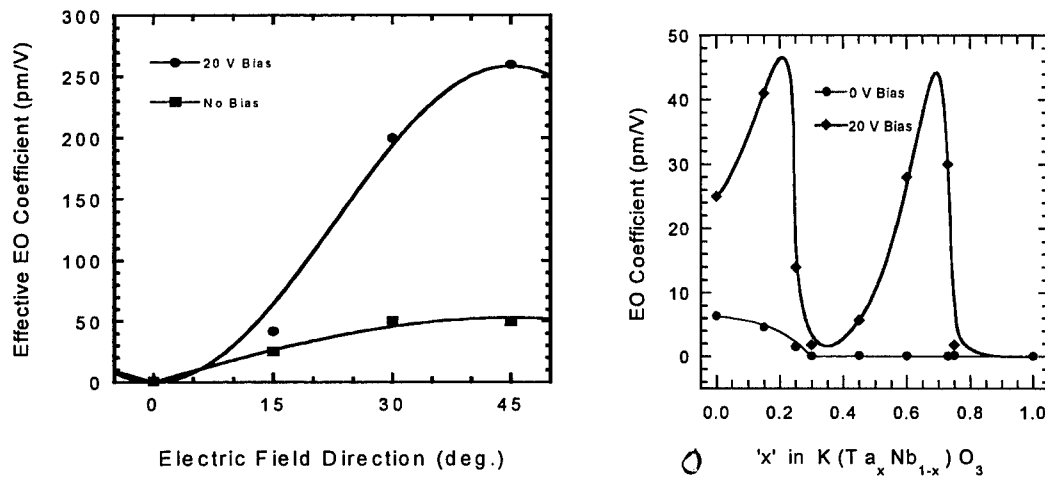

Figure 3   Left – EO coefficient plotted vs. field direction. Right – EO coefficient for $KTa_xNb_{1-x}O_3$ plotted vs. composition.

A material that shows considerable promise for high bandwidth modulators is $KNb_{1-x}Ta_xO_3$. In bulk materials electro-optic coefficients of 16000pm/V have been reported. We have investigated the EO properties of thin film $KNb_{1-x}Ta_xO_3$ prepared by MOVPE as a function of the composition. Substitution of Ta for Nb decreases the Curie temperature of the films. The material nominally has its highest EO effect at the Curie temperature. For unpoled films, however, the measured EO coefficient showed a monotonic decrease with increasing Ta%. Nevertheless EO coefficient measurements made with a bias field did show an increase for films with a composition of ~75% Ta. This is the composition where the Curie transition is approximately at room temperature. Figure 3(Right) shows the measured EO coefficient as a function of composition. This effect has been attributed to the "soft" domain structure of FE materials near the Curie transition.
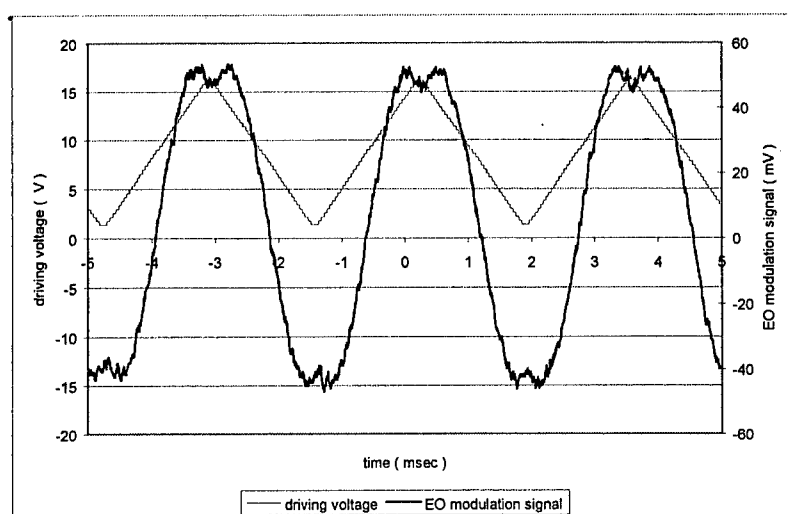
Ferroelectric waveguide electro-optic modulators have been fabricated from $BaTiO_3$. A lower switching voltage (V_π) has been achieved from this material system by fabricating waveguide whose propagation direction is in 45° with respect to the substrate crystal direction. The $BaTiO_3$ is deposited on MgO <100> substrate (a-axis normal to the substrate) by MOCVD method [10]. The resulting $BaTiO_3$ thin film has a multi-domain structure. Because MgO has four-fold symmetry with respect to its c-axis, crystal direction of $BaTiO_3$ in each grain is either <100> or <010> [9]. Previously, waveguides have been formed in <010> direction with coplanar

electrode geometry. In this case the responsible EO coefficients for the phase modulation are r_{33} or r_{13}, where $r_{33} \approx 97$ and $r_{13} \approx 19 \text{pm/V}$ for bulk $BaTiO_3$. However, the EO coefficient related to the TE wave propagation in <011> is r_{42} and its value is 1640. Therefore, it is expected to have a lower switching voltage if one fabricates a waveguide in <011> direction with proper electric field direction. Using this method, we have achieved switching-voltage length product, $V \cdot L = 5.2$ V·cm, for a waveguide in <011> direction, which is 3 times lower than that for a waveguide in <011> direction.

Epitaxial $BaTiO_3$ thin films were prepared by a low-pressure MOCVD process. Barium (hexafluoroacetylacetonate)$_2$ (tetraglyme) and titanium iso-propoxide were used as the precursors for barium and titanium, respectively. Oxygen saturated with de-ionized water was the oxidant. The films were deposited on (100) MgO at a growth temperature of 725°C. X-ray diffraction indicated that the films were epitaxial and had their crystallographic a-axis (100) aligned normal to the plane of the film. The thin-film $BaTiO_3$ sample was polished to reduce surface scattering loss and then divided to two pieces. 4µm-wide waveguides were patterned on both pieces of the samples by photolithography and 50nm thick waveguide ridges were defined by 5% diluted HF solution. Each sample has different waveguide orientation with respect to the MgO substrate crystal. One waveguide is along <010> direction of MgO substrate and the other is along <011> direction. 0.3µm-thick Au electrodes were fabricated on both samples by e-beam evaporation and lift-off technique. Its width is 100µm and the gap between the electrodes is 13µm. Both of the EO modulators were cleaved 3.5mm long.

A single mode $\lambda = 1.55$ µm laser with input power of 120µW was used to measure the EO modulation response. The end-firing method was used for coupling of the laser light into the $BaTiO_3$ ridge waveguide. Optical throughput for waveguide in the <010> direction is 3.5% for the TE and 0.4% for the TM mode. For the waveguide in the <011> direction, the optical throughput is lower than the waveguide in the <010> direction due to difficulties in cleaving. However, throughput ratio between the TE and TM modes is 1:1.

For these measurements, the input polarization is 45° from the normal to the sample and analyzer was at -45° to form a cross-polarization geometry. Therefore, electro-optically induced phase shift difference between the TE and TM waves results in intensity modulation of the output. The resulting intensity modulation is shown in Figure 4, where saw-tooth waveform is applied to the electrodes. From modulators of length 3.5 mm, switching voltage of ~50V is observed from the waveguide in <010> direction and ~15V for the waveguide in <011> direction. This corresponds to $V_\pi \cdot L$ of ~17.5 V·cm and ~5.2 V·cm, respectively. The effective EO coefficients are estimated to be 10.6pm/V and 35.3pm/V, respectively.

(a)
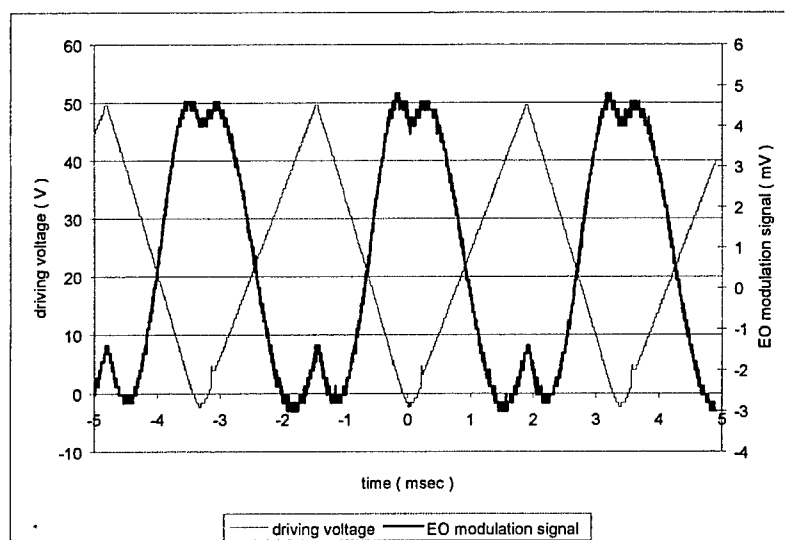
(b)

Figure 4   Switching voltage measurements of $BaTiO_3$ electro-optic modulators; (a) waveguide
in <010> direction, (b) waveguide in <011> direction.

1.3   Development of Er-doped thin film optical amplifiers

The research centered on improving the luminescent efficiency of Er doped $BaTiO_3$ thin films for use as integrated optical amplifiers. The Er doped films emitted at 1.54 microns. Inhomogeneous line broadening of the emission was noted. Factors leading to luminescence quenching and inhomogeneous broadening were studied.

The role of Auger processes in quenching of the Er luminescence was investigated. Er is nominally an electrical donor in BaTiO$_3$, thus a possible luminescence quenching mechanism is the Auger process involving free and bound electrons. To minimize the presence of free electrons the films were co-doped with the acceptor Al. Aluminum-doping was achieved by doping during thin film deposition where the Al source was aluminum acetylacetonate. The Al concentration was varied between 1 and 6 atomic per cent while the Er concentration was kept constant at 1%.

Photoluminescence measurements using a 980nm pump showed there was no significant improvement with Al doping in the Er emission intensity at 1.540 microns. The emission peak linewidth was also slightly broader in the Al co-doped samples. The experiments indicate that Auger processes are not the predominant quenching mechanism and that other processes need to be considered.

The role of upconversion and resonant transfer was subsequently considered. To limit upconversion co-doping with europium ions was investigated. The Eu^{3+} ions provide a pathway to depopulate the second excited state of Er^{3+} ion through resonant energy transfer and thereby increase the probability of 1.540-micron emission. Eu co-doping experiments were carried out for two different Er concentrations. The 1.540-micron emission intensity increased by a factor of 3 when co-doped with Eu. Figure 5(Left) shows the Er emission spectrum for the Eu co-doped sample and the undoped control sample.
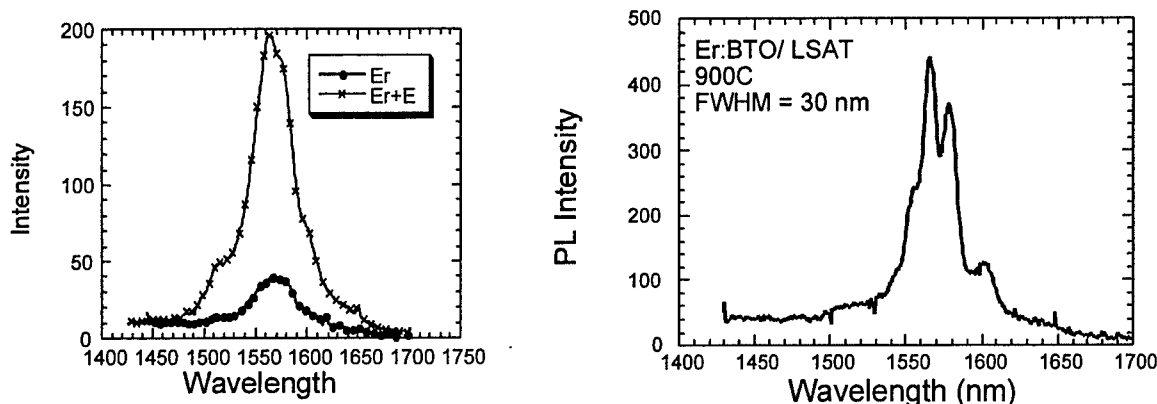

Figure 5   Left – Effect of Eu doping on Er emission intensity. Right – Er emission for barium titanate grown on LSAT. Decreased inhomogeneous line broadening is observed.

The factors leading to inhomogeneous line broadening were investigated. The Er emission in BaTiO$_3$ thin films typically shows significant inhomogeneous line broadening. Broadening is attributed to Er occupying several sites within the BaTiO$_3$. Secondly broadening due to residual strain is also a factor. To study the role of residual strain on line broadening films were deposited on substrates having differing degrees of lattice mismatch with respect to the film. The substrates used in this study were MgO (lattice mismatch = 4-5%), SrTiO$_3$ (lattice mismatch = 2-3%), and LSAT (lattice mismatch = 3-4%). For films deposited on substrates with lower mismatch an im-

provement in the crystalline quality was observed. The x-ray diffraction data indicates that films with lower strain can be obtained by depositing on LSAT. The lowest FWHM value for the x-ray rocking curve obtained on LSAT was 0.3°. The lowest FWHM was obtained for films on SrTiO$_3$ substrates for a growth temperature of 940°C; the rocking curve was 0.15° wide. This is the lowest FWHM measured to date for these films.

To determine the effect of strain on emission line broadening, the erbium emission was measured for films deposited on the different substrates. Figure 5(Right) shows the 1.54 emission for a growth at 850°C for BaTiO$_3$ on MgO and LSAT. Unlike films deposited on MgO, several well-resolved peaks are observed. The Er emission bandwidth is 20nm for the film on LSAT and 40nm for films on MgO. This finding strongly suggests that strain in the films is responsible for the observed emission peak broadening. By minimizing the strain, lower inhomogeneous broadening should result. This finding has implications in improving the gain of waveguide amplifier devices fabricated from the BaTiO$_3$ films.

1.4 Integration of epitaxial ferroelectric waveguide structures on silicon using metalorganic molecular beam epitaxy (MOMBE)

The work on the integration of epitaxial ferroelectric thin film waveguides on silicon continued. In order to realize epitaxial ferroelectrics an epitaxial oxide buffer layer on silicon is required. The buffer layer serves as a template for ferroelectric layer growth. It also serves to electrically and optically isolate the ferroelectric film from the silicon substrate. The work centered of optimization of the buffer layer growth by MOMBE and the subsequent growth of BaTiO$_3$ by MOVPE.
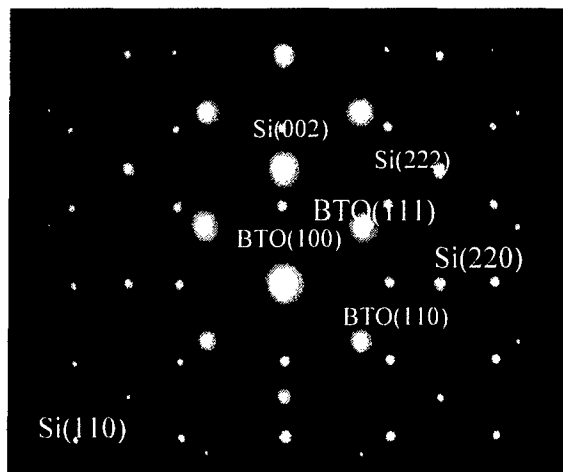

Figure 6   Selected area transmission-electron diffraction pattern for barium titanate on silicon.

MgO buffer layers on Si were deposited in a SVT Associates SN35 MBE system equipped with a load-lock, low temperature effusion cells and an RF oxygen plasma source. The solid metal-organic precursor Mg (acac)$_2$ (acac = acetylacetonate) was the source. Epitaxial cubic MgO thin buffer layers have been deposited on single crystal Si (001) substrates by MOMBE. The growth process involved initial formation of an epitaxial β-SiC interlayer followed by direct deposition of a MgO overlayer. Efforts were centered on growing MgO buffer layers with suffi-

cient thickness and crystalline perfection so that high quality ferroelectric layers could be subsequently grown. Films with a thickness of greater than 0.2 microns are needed. It was found, however, that for MgO films of 50 nm in thickness or less the layers were epitaxial and single crystalline. For larger thickness, the films became polycrystalline.

To test whether or not the MgO films on Si were of sufficient quality to serve as templates, a series of $BaTiO_3$ films were grown. Epitaxial $BaTiO_3$ films have been successfully grown on the MgO buffered (001) Si substrate by conventional MOVPE. The crystalline perfection of the films was assessed by x-ray diffraction. X-ray diffraction measurements indicated the $BaTiO_3$ films were epitaxial and a-axis oriented. This is the same orientation obtained when $BaTiO_3$ was deposited onto single-crystal (001) MgO substrate. Figure 6 shows a selected area TEM diffraction pattern from a region covering both Si substrate and the BTO film taken along Si (110), which indicates that the BTO and underlying Si has an epitaxial relationship given by BTO{100}//Si{002} and BTO{011}//Si(220). Figure 7 shows a TEM cross-sectional micrograph from the BTO/MgO/SiC/Si heterostructure. BTO showed a columnar growth with a faceted surface. The best BTO grown on the MgO/SiC-buffered Si by MOVPE has FMHW rocking curve width of 1.7° with a surface roughness of 8nm. Experiments to improve both buffer layer quality and ferroelectric layer quality are underway.

Figure 7   TEM cross-section micrograph of barium titanate on silicon.

The ferroelectric properties of the integrated $BaTiO_3$/MgO/Si heterostructures were evaluated. Figure 8 shows a P-V hysteresis loop for a 200nm thick BTO film grown on Si. The presence of hysteresis indicates that the grown film is ferroelectric although weak. Saturation of the polarization was not observed because of bias limitations. The presence of ferroelectric properties indicates that the films should show the electro-optic effect. This work indicates that formation of ferroelectric waveguide devices on silicon is possible.
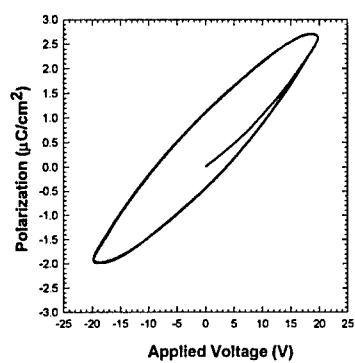
Figure 8   Polarization vs. bias for BaTiO₃ film grown on silicon.

2 Realization of Nanoscale Waveguide-Coupled Microcavity Resonators

High-Q microcavity resonators coupled to nanoscale waveguides will be of great interest to optical communications. We have demonstrated the fabrication of such resonators with GaAs/AlGaAs materials. In order to realize electrically tunable resonators at 1.55 microns, it is important to fabricate such resonators using InP/InGaAsP materials besides the GaAs/AlGaAs materials. This is because the required modulation voltage can be lowered by having the bandgap energy close to 1.55 microns. In addition, we explore methods to increase the Q of the resonators. One such method involves making a thinner modulator, which reduces the surface area of the etched sidewall, thereby reducing the scattering loss.

The program objectives for this part of the research program included:

- The fabrication of InP/InGaAsP micro-resonators coupled to nanoscale waveguides.
- Development of wafer bonding and back-etching technique to realize thin-film resonators based on InP/InGaAsP and GaAs/AlGaAs material systems.
- Study the optical losses in the thin-film resonators.
- Study the optical losses in thin-film nanoscale waveguides.
- Develop electrically tunable modulators.

Accomplishments:

2.1 Brief description

We have improved significantly the characteristics of channel add-drop filters based on the InGaAsP/InP thin film microcavity resonators coupled to nanoscale waveguides. This work is the first demonstration of a working device using InGaAsP/InP system, which is more difficult to fabricate than AlGaAs/GaAs system. Thin film nanostructures are made using standard nanofabrication techniques as well as a newly developed polymer wafer bonding technique, which is to provide two-dimensional strong optical confinement. The significantly higher performance of this add-drop filter comes from the improvement of the polymer wafer bonding process, which subsequently lowers the waveguide propagation loss and increases the microcavity Q value. The optical propagation loss is measured to be less than 0.7 cm^{-1} for both the TE and TM cases, which is three times less than the previous results. The transmission spectrum of a 10-μm disk resonator shows that the Q of microdisk cavity is as high as 7000. This result is encouraging and considered being one step closer to the practical application in the optical Dense Wavelength-Division-Multiplex (DWDM) system network.

2.2 Design and fabrication

The geometry of our microdisk resonators with coupling waveguides is the same as that in Ref. [12]. The wafer structure with a 0.4 μm-thick InGaAsP ($\lambda_g = 1.2 \mu m$) guiding layer is grown on an InP substrate by molecular-beam epitaxy [Figure 9(left)]. To prepare the epitaxy sample for etching, a 400nm-thick SiO$_2$ layer was deposited by plasma enhanced chemical vapor deposition (PECVD). This SiO$_2$ layer acts as a hard mask for etching. The wafer is then patterned through a soft mask of 180nm-thick 2% polymethylmethacrylate (PMMA) using electron-

beam lithography. The pattern on the PMMA mask was subsequently transferred to the underlying SiO$_2$ layer using reactive-ion etching (RIE). Dry etching utilizing inductively coupled plasma (ICP) with a gas mixture of Cl$_2$: Ar$^+$ (2:3) was employed to transfer the pattern onto the epitaxy wafer through the SiO$_2$ hard mask at an elevated temperature of 250^{0}C. The etching depth was about 1.3 μm. After the etching process, we removed the SiO$_2$ hard mask using buffered HF. Finally, the devices were transferred to a GaAs substrate via a polymer bonding technique, which is described in the following section. A scanning electron micrograph of a 10 μm -disk resonator with coupled waveguide is shown in Figure 9(right).

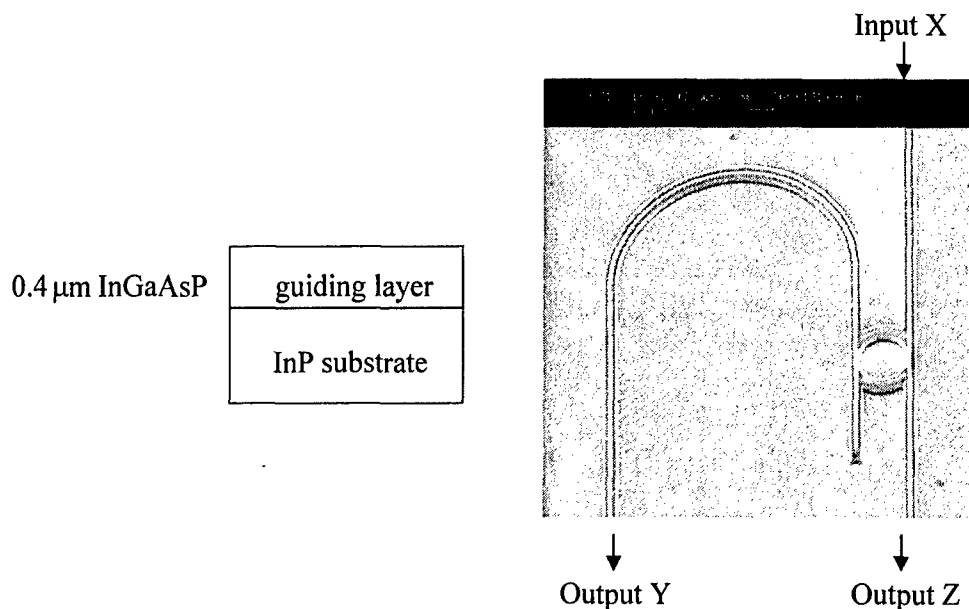

Figure 9:   Left – Illustration of the InP/InGaAsP wafer structure. Right – SEM image of a 10 μm -disk resonator with coupled waveguide after BCB bonding.

2.3 Improved polymer bonding process

In a progress report, we described a polymer bonding process, which utilizes the polymer Benzocyclobutenes (BCB) to bond the semiconductor wafer to another substrate [13]. During the last funding period of this project, we improved this polymer bonding process and achieved high quality bonded waveguides and microcavity resonators. The improvements are due to:

1. We use a more diluted BCB solution cyclotene 3022-35 instead of 3022-46. By using 3022-35, we can have a more uniform and thinner BCB film, which helps to remove the bubbles and makes the cleaving easier.

2. Before annealing, we put the bonded wafer on the hotplate at a temperature of 120°C for a while. At this temperature, the BCB becomes less viscous, which allows us to make initial alignment of the wafers. In addition, this helps to remove the bubbles trapped between the wafers.

3. We have divided the annealing process into more segments, which allow slower temperature increase, and longer annealing time. The annealing temperature is also increased from 250°C to 270°C. Under the new annealing process, the BCB film is more fully cured and therefore becomes more resistant to the solvents.

4. The backside etchant has been changed from HCl:H₃PO₄ to non-diluted HCl. The etching rate of HCl is much faster and the selectivity is higher. The etched surface is also much cleaner.

Based on this improved polymer bonding process, we have successfully fabricated BCB bonded nano-scale waveguide with propagation loss less than the previous results. The loss measurement was again performed by the cutback method as we described in the last report. The results for a waveguide tapered from $2\,\mu$m to $0.8\,\mu$m are given as below:

$$\text{TE: } \alpha = 0.77 \text{ cm}^{-1}, R = 20.7\%$$

$$\text{TM: } \alpha = 0.65 \text{ cm}^{-1}, R = 21.2\%$$

The current results on loss are almost one third of our previous results.


2.4 Reflectivity and Transmission measurement

The methods for the waveguide coupling and reflectivity & transmission measurement are similar to those reported last time and can also be found in Ref. [14]. The reflection spectra for the TE and TM modes of a $10\,\mu m$-diameter BCB bonded microdisk resonator are shown in Figure 10 (the TE polarization is parallel to the substrate). For the TE case, there are 3 sets of resonance modes. Each set has a FSR $\Delta\lambda_{fsr} \approx 21$nm with a full-width at half maximum $\delta\lambda_{FWHM} \approx 0.25$nm, which results in a finesse of 84. For the TM case, we have 2 sets of resonance modes with $\Delta\lambda_{fsr} \approx 20$nm and $\delta\lambda_{FWHM} \approx 0.22$nm, which gives a finesse of 91. Note that the presence of the multiple sets of resonance modes is due to the guiding layer not being single mode waveguide. Therefore, higher-order modes could be excited in the disk resonator. The large FSR is due to the small diameter of the disk and the narrow linewidth is due to the low cavity loss. In microdisk resonators, whispering gallery modes (WGMs) can have high Q values, where $Q = \lambda/\delta\lambda_{FWHM}$. In our case, both the TE and TM resonance modes show Q value as high as 8000.

The reflectivity r has also been calculated using the conformal transformation and WKB approximation as described in [15,16]. The simulated results are shown in Figure 11 from which we see that the resonance wavelengths match the experimental data reasonably. Note that the TE modes suffer more losses than the TM modes in our devices. This is probably due to larger scattering loss in the TE-mode case.

From Figure 10, one can estimate that the maximum transmissivity is ~40% for the TE and ~90% for the TM case, respectively. Figure 11 shows the measured transmissivity from port Y for the TM case. Compared with Figure 10(b), we can see that $t_{max} \approx 1 - r_{min}$ for most of the resonant wavelengths, which means that the total loss from the disk resonator and the coupling
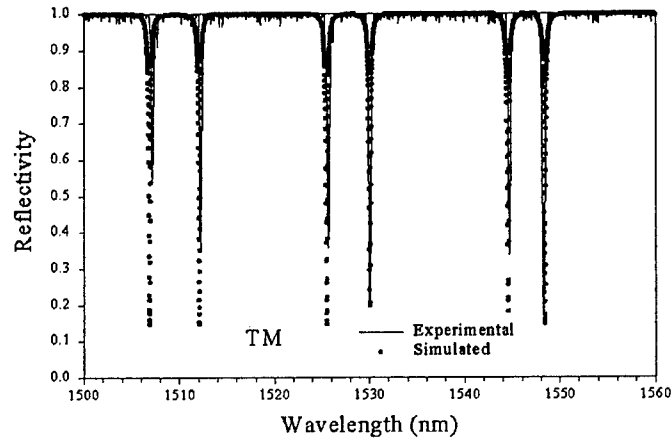
(a)
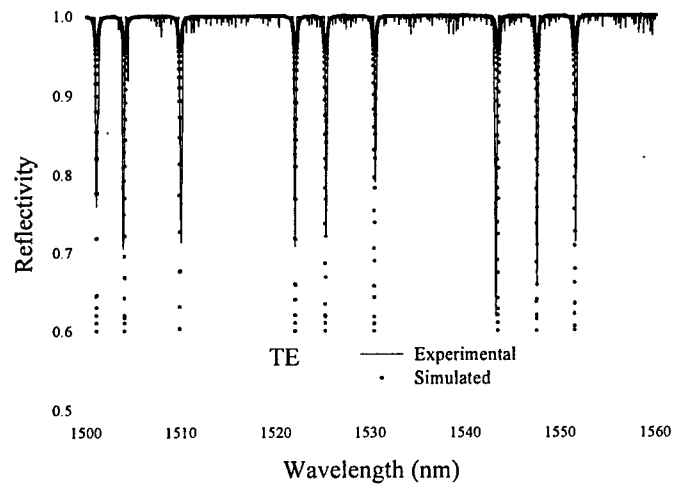
(b)

Figure 10   Reflectivity as a function of wavelength of a 10 μm -diameter BCB bonded micro-disk resonator. ——— Experimental, …… Simulated for (a) TE (b) TM.

waveguide is small. The TE case has similar results. We estimate the total loss to be about 0.7dB for a $10\,\mu m$-diameter disk resonator and 1mm-long tapered coupling waveguide [17]. Almost 90% transmission near 1545nm shows bright future for this device as a practical device. However, wavelength dependence of the transmission peak has to be further investigated.
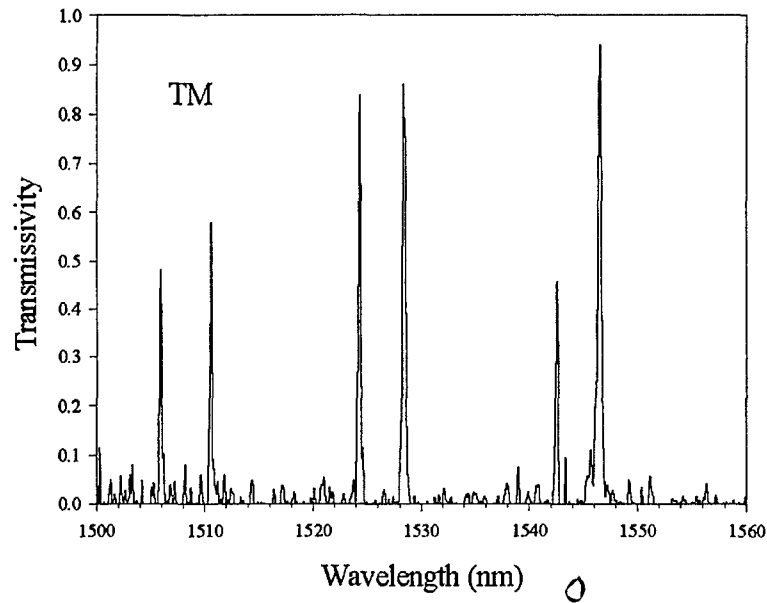

Figure 11 Measured transmissivity as the function of wavelength of a $10\,\mu m$-diameter BCB bonded microdisk resonator for the TM case.

3   TDM Applications of Fiber-optic Parametric Nonlinearities

In this part of the MURI our emphasis was on component integration with the goal of developing modules for deployment in the aforementioned TDM optical networks. In particular, we worked on exploiting the parametric nonlinearity of the standard telecommunication fiber excited by mode-locked fiber lasers to demonstrate functionalities that will be needed in the all-optical networks. During the last two funding periods we developed a tunable fiber-optic clock-recovery scheme [34], demonstrated an all-fiber limiting amplifier [27], and a novel all-optical storage buffer capable of storing 20Gb/s data packets for up to several seconds [35]. Below we describe these in detail.

Accomplishments:

3.1   Wavelength-tunable all-optical clock recovery using a fiber-optic parametric oscillator

We have reported a wavelength-tunable clock recovery scheme for all-optical 3R regeneration and simultaneous wavelength conversion [34]. The scheme is based on a fiber-optic parametric oscillator, in which dynamic gain results from the four-wave mixing process in the fiber. In our implementation, 2.9ps clock pulses are recovered from the incident pseudo-random data stream with the clock wavelength being tunable over the whole EDFA bandwidth. RF spectrum measurements show that the recovered clock has less timing jitter than the incident data stream. We have also carried out a two-channel clock recovery experiment, which demonstrates the feasibility of our scheme at 100Gbit/s data rate.

Future ultrahigh-speed optical networks will operate with terabit/s aggregate capacity using wavelength-division multiplexing (WDM) at very-high data rates per channel. All-optical wavelength conversion is expected to be a key component in such systems in order to provide for network re-configurability, non-blocking capability, and routing functions. There have been many approaches to realize wavelength conversion, such as cross-gain modulation (XGM) [18], cross-phase modulation (XPM) [19], and four-wave mixing (FWM) [20], all in semiconductor optical amplifiers (SOAs). However, when data streams go through fiber links and wavelength-conversion nodes, signals are impaired by the amplified-spontaneous-emission (ASE) noise, timing jitter, FWM crosstalk, polarization mode dispersion (PMD), and other practical factors, which limit the transmission distance, and therefore the network scale. For example, with FWM as the wavelength-conversion mechanism, the transmission distance in a WDM cross-connect network is a few hundred kilometers at 10Gbit/s [21]. Re-amplifying, reshaping, and re-timing, i.e., 3R regeneration of the data is required to break this limit. A wavelength-tunable clock recovery is very promising for constructing a wavelength converter with simultaneous 3R regeneration. Figure 12(Left) shows a schematic block diagram of a 3R wavelength converter that consists of a tunable-wavelength clock recovery followed by an optical switching gate, which is on-off modulated by the data pulses. Since the same data pattern is copied onto the clock pulses, the output of the switching gate is 3R regenerated data pulses with simultaneous wavelength conversion. The optical switching gate could be a nonlinear optical loop mirror [22] or a SOA

interferometer [23]. The fidelity of the recovered clock in this scheme determines the performance of the 3R-regeneration cum wavelength-conversion process.
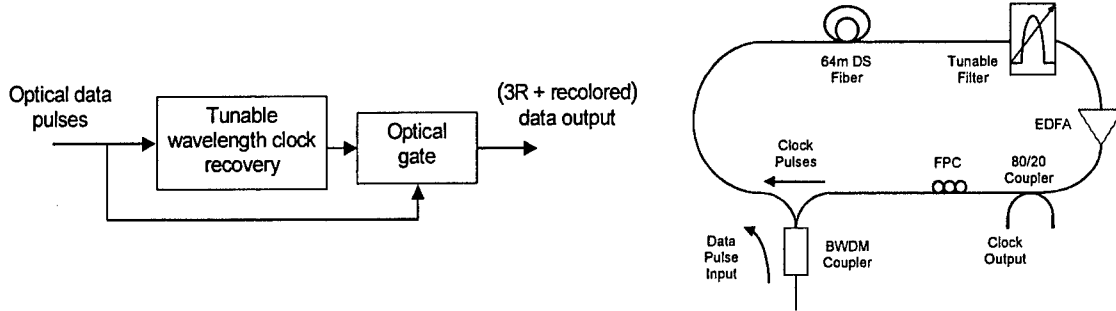

Figure 12   Left: A schematic block diagram of a 3R regenerator cum wavelength converter.
            Right: A schematic of our wavelength-tunable clock recovery setup.

In our work, the wavelength-tunable clock recovery scheme is based on a fiber-optic para-metric oscillator (FOPO) in the ring configuration. The fundamental data-rate limitation in this scheme is the time response of the Kerr nonlinearity of the fiber, which is in the femtosecond range compared to the sub-nanosecond range offered by the SOA-based clock recovery schemes (e.g., the figure-eight laser [24]). As a result, our clock recovery system is expected to be scal-able to data rates that are in the terabit/s range. In addition, the recovered clock is wavelength tunable over the whole erbium-doped-fiber-amplifier (EDFA) bandwidth. Therefore, this system also realizes wideband wavelength conversion. The key part of our system is a singly resonant FOPO [25] that is pumped by fixed-wavelength picosecond pulses. A tunable filter selects the desired wavelength of the clock pulses, which are generated by means of the FWM process in the FOPO.

A schematic diagram of our experiment is shown in Figure 12(Right). The FOPO is config-ured as a ring cavity in which a tunable filter (3nm pass-band width) selects the desired oscillat-ing wavelength. The oscillating signal is amplified by an EDFA to compensate for the ring-cavity loss. An 80/20 coupler splits out 20% of the oscillating-signal power as the clock output. The remaining 80% of the signal is passed through a fiber-polarization controller (FPC), which is adjusted to compensate the birefringence of all the fiber in the ring cavity. A 64m-long piece of dispersion-shifted (DS) fiber (λ_0 = 1537nm) is the FWM medium. The input data pulses, which act as pump pulses for the FWM process, are coupled into the FOPO cavity by means of a band-pass wavelength-division multiplexer (BWDM). The BWDM and the isolator in the EDFA en-sure a unidirectional ring cavity, in which forward FWM occurs. The ring-cavity length is ad-justed in such a way that the FOPO, which is singly resonant, is harmonically mode locked ow-ing to the FWM-gain modulation provided by the pump pulses. When all the pump pulses are present, i.e., the input data is all *ones*, the system works just like a pulsed FOPO [25] (configured here as a ring cavity instead of the linear cavity as in Ref. 25). It is self-starting; the oscillating pulses build up from the ASE noise in the ring cavity, while the tunable filter selects the desired wavelength. However, when the pump pulses are in the form of a random data stream, the FOPO still oscillates as long as the EDFA gain is adjusted to compensate for the total ring-cavity loss, which is estimated to be 6.5dB in the setup of Figure 12(Right). In our experiment, the data stream is a 2^7-1 pseudo-random sequence of pulses obtained by modulating the output of a pas-sively mode-locked (PML) Er:Yb-fiber laser. The laser produces ~5ps FWHM sech-shaped

pulses at a repetition rate of 14.14MHz and the center wavelength is 1541.5nm. The repetition rate of the laser is slightly adjustable; allowing it to be precisely set an integral multiple of the FOPO-cavity free-spectral range.
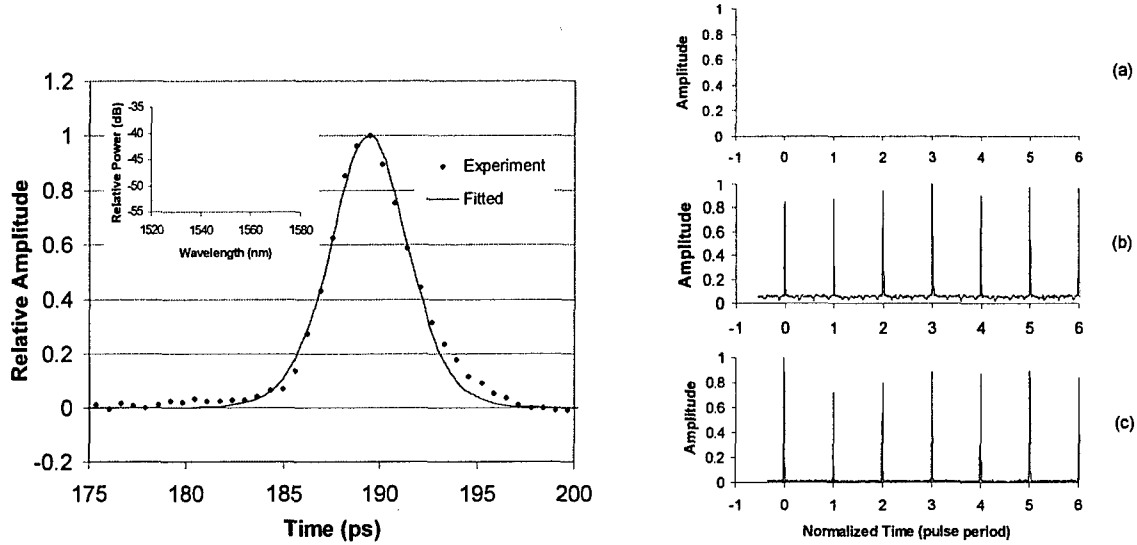
Figure 13   Left: Autocorrelation signal of the output clock pulses at 1555nm. Slight asymmetry of the measured data points is an artifact; the detection time constant in the autocorrelator was inadvertently not set sufficiently short. The inset shows composite optical spectra of the clock pulses for two different filter settings. Right: A sample of the input pseudo-random data pulses, (a), and the recovered clock pulses at 1534nm, (b), and 1555nm, (c), respectively. The time scale is normalized to the pulse period. The amplitude fluctuation is an artifact (see text) and in (b) the higher baseline results from some CW lasing in the FOPO cavity.

In order to get stable clock pulses the gain of the EDFA needs to be finely adjusted. It should compensate most of the ring-cavity loss, but should be set below the threshold of CW oscillation in the ring cavity. The dynamic FWM-gain window created by the pulsed pump provides the mode-locking mechanism. In our experiment, the pump current to the EDFA can be adjusted in 0.5% increments, which was found to be adequate for the required EDFA gain control. Since the EDFA gain is maintained below the round-trip loss, XPM alone, caused by the pump pulses, cannot lead to mode locking. Indeed, when we tapped a small portion of the oscillating signal at a point between the DSF and the filter, we found clear evidence of the presence of the generated idler component, which is blocked by the filter. For 1.5mW of average pump power, the average output power of the clock pulses was around 5μW. In Figure 13(Left), we show an autocorrelation trace of the recovered clock pulses when the clock wavelength was tuned to 1555nm. The solid line is a fitted curve based on Sech^2-intensity profile for the recovered clock pulses, which turn out to have 2.9ps FWHM. The clock pulses are tunable as shown by the inset in Figure 13(Left), which displays a composite of the optical spectra of the clock pulses for two different settings of the intracavity filter. The clock wavelength was continuously tunable over the whole EDFA bandwidth (from 1532 to 1562nm), except the notch band of the BWDM coupler, which is 3nm wide and centered on the pump wavelength. In such FOPO-based clock recovery, the inherent tunability range is limited by the FWM-gain bandwidth, which is determined by phase-

matching considerations. In the fiber parametric amplification process, only even dispersion orders affect the gain [26]. If the DS fiber is pumped at the zero-dispersion wavelength, to lowest order only β_4 affects the FWM-gain bandwidth, which can be several 10's of nanometers wide [26].

In Figure 13(Right), we show a sample of the input pseudo-random data pulses at 1541.5nm, and the recovered clock pulses at 1534 and 1555nm, respectively. We measured the pulses by a high-speed (>2GHz bandwidth) photodetector and recorded them with use of a digital oscilloscope having 4-GHz sampling rate. The amplitude fluctuation appearing in Figure 13 is thus an artifact, owing to only a few data samples captured by the oscilloscope during each pulse. We attribute the amplitude stability of the recovered clock pulses to FWM-gain saturation owing to depletion of the pump (incoming data) pulses. Gain saturation allows a weaker pulse to see more gain than a stronger pulse [27]. Thus when a *zero* arrives (i.e., no pump pulse), the coincident recovered-clock pulse sees no FWM gain and hence sees net loss in the subsequent round-trip around the ring cavity. However, this weaker clock pulse will see larger FWM gain on the next round trip than the average gain if a *one* arrives. Therefore, FWM gain recovery stabilizes the clock pulses in response to the arrival of a moderately long (6 consecutive *zeros* in our experiment) string of *zeros*. During successive *zeros*, the clock-pulse amplitude decays exponentially. The time constant is determined by the net round-trip loss in the FOPO cavity. This decay, however, can be minimized by setting the EDFA gain as close to (but below) the cavity round-trip loss as possible. In response to a long string of *ones*, the clock-recovery setup performs exactly as a FOPO, whose output has negligible pulse-to-pulse fluctuation.
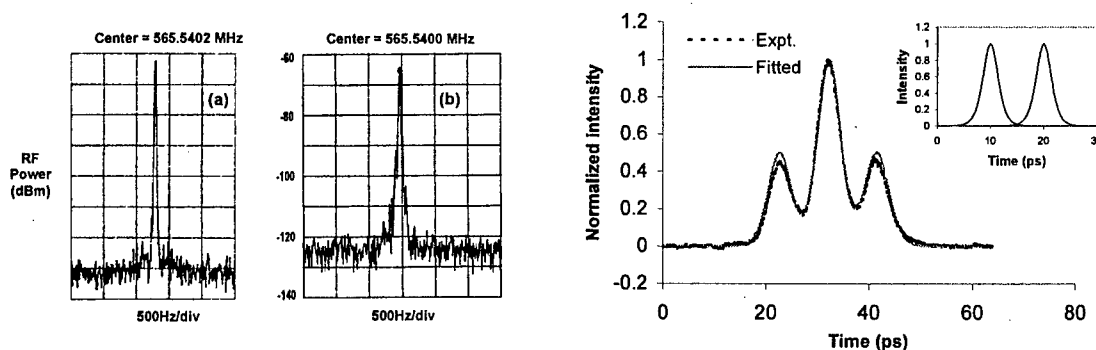

Figure 14   Left – RF spectra near the 40th harmonic of the data rate for the recovered clock, (a), and the source laser, (b), recorded with 10Hz resolution and video bandwidths. Right – Autocorrelation trace of clock pulses recovered from two TDM channels with 10ps spacing. Solid line is a fit using the clock-pulse pair shown in the inset.

We have also investigated the timing-jitter performance of the recovered clock pulses by analyzing their photocurrent spectrum upon direct detection [28]. In Figure 14(Left)(a), we show a portion of the RF spectrum near the 40th harmonic of the data rate. Upon comparison with Figure 14(Left)(b), which shows similar spectrum for the PML fiber-laser source, we see that the phase-noise sideboards in the wings of the 40th harmonic are substantially reduced. Thus, we conclude that the recovered clock pulses have much less timing jitter than the injected data stream. The reduction of the timing jitter can be qualitatively understood by noting that the clock pulses are generated within the average FWM-gain window created by the data pulses. Finally,

by properly setting the intracavity FPC, we were also able to observe that the performance (i.e., the amplitude stability and the timing jitter) of this clock-recovery system is insensitive to the polarization-state of the input data pulses. The polarization-state of the output clock pulses, however, varies as the polarization-state of the input data stream changes.

In order to investigate the clock-recovery performance at 100Gbit/s, we created two time-division-multiplexed (TDM) channels with 10ps spacing using a fiber delay-line multiplexer. The length of the delay branch in the multiplexer is chosen to be 14.3m, thus assuring decorrelation of the two adjacent channels. In this way, a pseudo-random sequence of 10ps-separated pulse pairs (10, 01, 00, and 11 with equal probabilities) is injected into the FOPO cavity. In Figure 14(Right), we show the autocorrelation trace of the recovered clock pulses with such injection of two TDM channels. The side peaks, which are 10ps away on either side of the central peak, are almost half as high as the central peak. Such half-height side peaks are expected in the autocorrelation signal of a train of pulse-pairs. Slightly lower peaks in our experiment result from a relative polarization shift in the two branches of the delay-line multiplexer, causing the two channels in the output clock to have slightly different polarization states, which in turn leads to a reduced autocorrelation signal. Thus, the data in Figure 14(Right) clearly shows that the clock pulses for both TDM channels are simultaneously recovered. The solid curve is a fit to the data with pulse pairs of 2.9ps FWHM and 10ps-center separation. In the inset, we display such a pulse pair, which shows that the overlap in the tails occurs at less than 2% of the peak power. Thus, our clock-recovery scheme would work without severe penalty if the input were a 100Gb/s data stream. Furthermore, we expect the scheme to work at even higher data rates, since the two TDM channels in Figure 14(Right) could be placed closer than 10ps if a source of narrower pulses is employed.

In practical implementation of a high-bit-rate clock recovery system, i.e., when data pulses fill all time slots, high average input power would be required to maintain the same pulse peak power. This requirement, however, can be met by using high nonlinearity fibers or glasses with nonlinearity 1000 times larger [29,30] than that of standard fiber, and commercially available high-power EDFAs for signal pre-amplification. It is thus possible to envision clock-recovery systems with bit rates approaching Tb/s. Such clock recovery has several useful features. Firstly, the single ring configuration is very simple and inherently suitable for integration if using high nonlinearity waveguides [29,30]. Secondly, most components are commercially available making the system cost effective. Thirdly, the idler pulses, instead of being filtered out, could be utilized for mid-span wavelength conversion to extend the transmission distance [31,32], which is an advantage of the present scheme over the XPM-induced mode locking based clock recovery scheme [22].

3.2 All-optical limiter using a gain flattened fiber parametric amplifier

We have reported an all-optical limiting amplifier that is capable of reducing amplitude fluctuation of 20Gbit/s data packets [27]. The limiting amplifier is based on a gain flattened two-stage fiber parametric amplifier having a record bandwidth of 15nm.

In high-speed dense wavelength-division multiplexing (DWDM) systems, the fiber nonlinearity induces inter-channel crosstalk due to processes such as four-wave mixing (FWM), cross-phase modulation (XPM), and stimulated Raman scattering (SRS) [36]. After a channel is de-

multiplexed, the received data stream may have severe amplitude fluctuation (particularly at marks), which increases power penalty for the receiver. An optical limiting amplifier is desired to suppress this amplitude fluctuation, which would then realize re-amplifying and reshaping functions simultaneously. The optical limiting amplifier has to be ultrafast for it to handle data rates at 40Gbit/s or higher. Fiber parametric amplifier (FPA) is an ideal candidate, because the limiting amplification mechanism is based on the ultrafast parametric-gain saturation in the fiber. Since the response time of the Kerr nonlinearity of the fiber is on the order of femtoseconds, an FPA can provide potential applications in the terabit/s range. The peak gain of a FPA can be very high if strong pump is available [37,25]. However, there is a drawback of using FPAs as general-purpose optical amplifiers. Although the FPAs can provide gain greater than one over a very broad range, the gain spectrum is not flat. Usually the 3-dB bandwidth of the FPAs is only a few nanometers. This severely limits the application of FPAs for amplifying signals at different wavelengths.

We have reported, for the first to the best of our knowledge, an all-optical limiter using a FPA. We have experimentally demonstrated reduction of amplitude fluctuation of 20Gbit/s packets using a two-section FPA having a 3-dB bandwidth of 15nm, which is a record bandwidth for an FPA to this date. Furthermore, for application in a wideband WDM system it is possible to employ multiple FPAs, each with different center wavelength for use on a given channel.
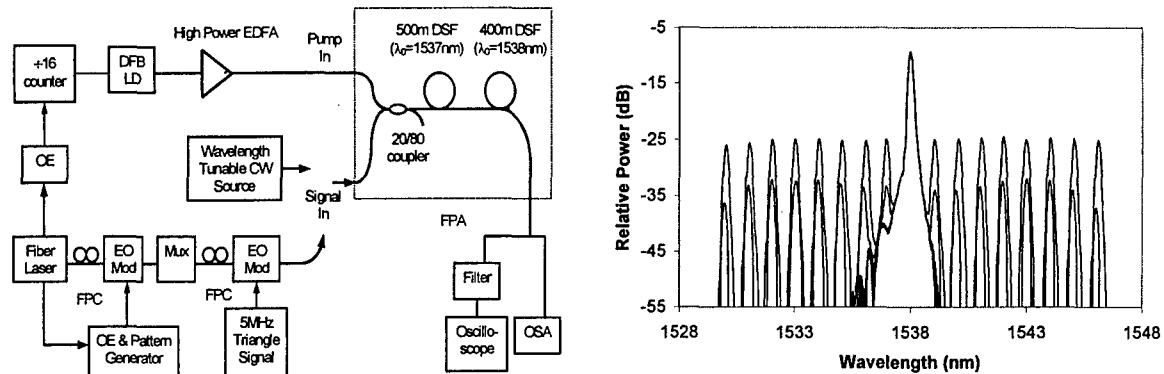
Figure 15   Left – Experimental setup to characterize the all-optical limiting amplifier. OE: Optical to electrical conversion, FPC: Fiber polarization controller, EO MOD: Electro-optical intensity modulator, Mux: optical multiplexer, DSF: Dispersion shifted fiber, FPA: Fiber parametric amplifier, OSA: Optical spectrum analyzer. Right – Composite spectra measured at the FPA output. Upper: Signal, Lower: Idler, Center: Pump.

The experimental setup for the gain flattened FPA is shown in Figure 15(Left). An electronic counter, which is synchronized to the 1542nm pulsed output of a 14.14MHz-rate fiber laser, produces 1/16 duty-cycle TTL pulses to drive a DFB laser diode of 1537.8nm wavelength. The quasi-CW output of the DFB laser is amplified by a two-stage high-power EDFA and used as a pump for the FPA. The high-power EDFA has a saturated output power of ~90mW; therefore the peak power of the quasi-CW pump is 1.44W before it is coupled into the dispersion-shifted fiber (DSF). A 20/80 coupler sends 80% of the pump power into our gain flattened FPA, which consists of two pieces of DSF with different lengths and zero-dispersion wavelengths (λ_0's). The peak power of the pump launched into the composite DSF is estimated to be 1W. The λ_0's were chosen such that for one λ_0=1537nm, slightly shorter than the pump wavelength, and for the

other $\lambda_0 = 1538$nm, slightly longer than the pump wavelength. With such choice, the two DSFs provide complimentary gain spectra. From simulation [29], we found the optimized lengths for having flattened gain spectrum to be 500 and 400m, respectively, for the $\lambda_0 = 1537$nm and $\lambda_0 = 1538$nm fibers.
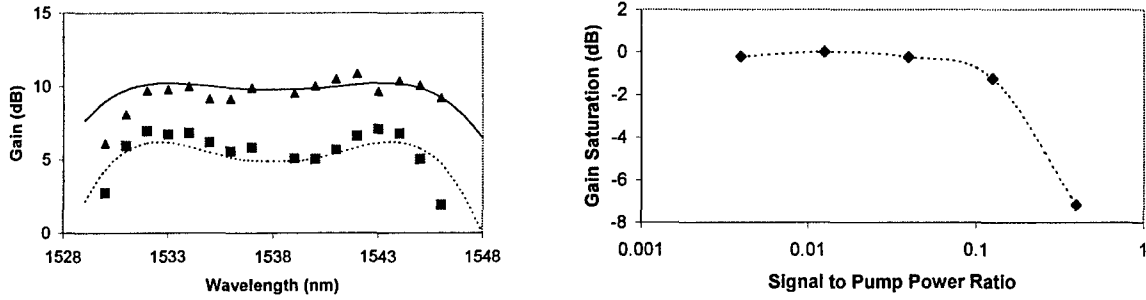

Figure 16   Left – Gain spectra of the signal and idler components. Triangles: Measured signal gain. Squares: Measured idler gain. Solid: Simulation of the small signal gain. Dashed: Simulation of accompanying idler gain. Right – Gain saturation characteristic of the FPA. 0dB saturation corresponds to small signal amplification.

To characterize the gain flatness of the FPA, we used a wavelength tunable CW source with a constant output power of 1mW to scan over the FPA bandwidth. We tuned the CW source from 1530nm to 1546nm with a step of 1nm. Figure 15(Right) shows a composite of the spectra taken at the output of the FPA. Since the pump is chopped with 1/16 duty cycle, only 1/16 of the CW input is amplified, corresponding to the upper traces in Figure 15(Right). At each signal wavelength, an idler component is generated simultaneously whose frequency satisfies $\omega_i = 2\omega_p - \omega_s$, as the lower traces show. The strong peak at 1537.8nm is the pump. The small-signal gain and the idler gain are obtained using $g_{signal} = 16 \times (P_{on} - P_{off})/P_{off}$, where P_{on} is the measured output-signal power when the pump is turned on [the upper traces in Figure 15(Right)] and P_{off} is the signal power with the pump off [not shown in Figure 15(Right)]. For the idler we have $g_{idler} = P_{idler}/P_{off}$. Figure 16(Left) shows the gain spectra of the signal and idler derived from Figure 15(Right) using the above formulae. The 3-dB bandwidth of the FPA is about 15nm, which is a record bandwidth of a FPA to this date to the best of our knowledge.

Gain saturation occurs when the signal is strong for it to deplete the pump. Figure 16(Right) is a plot of the measured gain for different input signal powers. As shown, the gain starts to drop when the signal-to-pump peak power ratio exceeds 0.1.

To demonstrate the limiting application of the FPA we used the fiber laser as the pulsed signal source. A 2^7-1 pseudo-random bit-pattern generator, which is synchronized to the fiber laser, on off modulates the ~5ps sech-shaped 14.14MHz-rate pulses from the fiber laser. We created two-bit packets using a fiber delay-line multiplexer. The length of the delay branch in the multiplexer is chosen to be 14.3m, thus assuring de-correlation of the two adjacent bits, which are spaced by 50ps. A second modulator is driven by an unsynchronized 5MHz triangular voltage source, causing the modulated packets to have about 40% amplitude fluctuation. The fluctuating 20Gbit/s packets are sent through the 20/80 coupler and 20% is coupled into the composite FPA.

The peak power of the signal pulses is estimated to be 100mW. After being amplified under the pump saturation condition, the output signal is filtered to remove the idler and the pump components. The filtered signal is monitored by a 20GHz-bandwidth photodetector and recorded by a sampling oscilloscope. Figure 17 shows the eye diagrams of the packets before and after the FPA. Clearly, the amplitude fluctuation is reduced. The bit spacing could be further reduced to demonstrate limiting amplification of higher bit-rate packets if a faster speed photodetector were available for the oscilloscope.
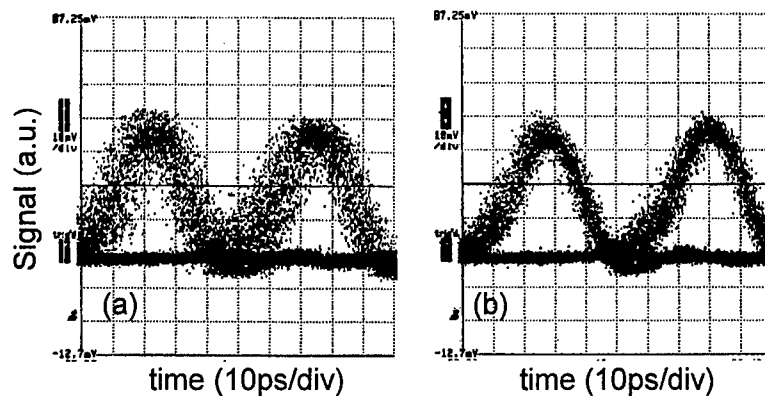

Figure 17   Amplitude fluctuation of the 20Gbit/s packets (a) before the FPA, (b) after the FPA. Sampling scope persistence time is 3s.

In summary, we have demonstrated, for the first time, an all-optical limiter using a gain flattened FPA. We achieved a record gain bandwidth of 15nm with a novel design of the FPA. By action of the dynamic parametric gain saturation, amplitude fluctuation of 20Gbit/s packets is dramatically suppressed by the FPA operating as a limiting amplifier. The long DSF length and the relatively high, injected pump power can be reduced by a factor of 10–1000 if high nonlinearity fiber or glasses are used [29].

3.3 An all-optical picosecond-pulse packet buffer based on four-wave mixing loading and intracavity soliton control

We have demonstrated a novel all-optical picosecond-pulse storage buffer by combining the synchronous parametric-gain modulation provided by a pulse-pumped nonlinear-optical loop mirror with the soliton shaping property of a nonlinear amplifying loop mirror [35]. A 20Gbit/s-packet pattern was stored for several seconds.

All-optical buffering is critical for optical/photonic packet switchers or IP routers to solve contention issues and for access nodes to bridge the speed gap. Several types of optical/photonic buffers have been demonstrated utilizing fiber re-circulating loops [39–41] and regenerative loops [42]. Conventional photonic re-circulating-loop designs [39,40] have employed EDFA or SOA to compensate the round-trip loss while electrically driven modulator is used to maintain the signal timing. In addition to the bit-rate limitation imposed by the speed bottleneck of electrical devices, these types of buffers suffer from serious extinction-ratio degradation of the stored

signal owing to the accumulated ASE noise. In this paper, we report a novel approach that is based on four-wave mixing (FWM) loading and intracavity periodic soliton control [43]. The target packet is loaded into the storage loop by means of the FWM interaction between the pump and signal pulses and stored as the resulting idler pulse train. The timing and amplitude of the stored pulses are stabilized by periodic soliton control [44] through synchronous parametric-gain modulation inside a pulse-pumped NOLM and the soliton shaping property of a NALM. A picosecond, 20Gbit/s-packet pattern is stored for up to seconds or millions of circulations in the storage loop.
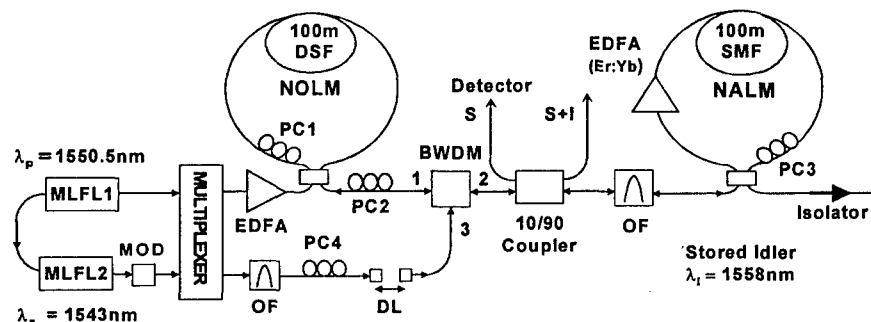

Figure 18   A schematic diagram of the experimental setup for the storage buffer.

Figure 18 shows a schematic diagram of the experimental setup. A NOLM and a NALM constitute a nonlinear Fabry-Perot (FP) cavity that acts as the storage buffer. A 3-port BWDM is used to inject/eject (1↔3) the signal packets into/out of the NOLM and to bypass (1↔2) the idler resulting from FWM inside the NOLM. A 3-nm bandwidth tunable filter and a 10/90 coupler are employed, respectively, to select the stored wavelength and to output the stored signal. Intracavity PC2 is utilized to make sure that after one round trip the state of polarization of the light is the same. The NOLM consists of a 100-m piece of dispersion-shifted fiber (DSF) with zero-dispersion wavelength at 1538nm. The DSF provides dynamic parametric-gain and phase modulation via the processes of FWM and cross-phase modulation (XPM), respectively, when pumped by picosecond pulses. The NALM is made of a 100-m piece of SMF-28 fiber spliced on one end to a 1-m piece of Er:Yb co-doped gain fiber and on the other end to a polarization controller (PC3). The PC3 can be adjusted to generate different linear-phase retardations for the counter-propagating waves inside the NALM.

The pump laser is a passively mode-locked fiber laser, which generates a 14-MHz train of 6.2ps transform-limited soliton pulses at 1550.5nm. Another fiber laser, which is synchronously mode-locked to the pump laser and generates a soliton stream of 5ps pulses at 1543nm, is used as the signal source. An amplitude modulator (AM) creates the 32-bit data packet, which consists of 8 ones followed by 24 zeros. For the high-speed experiment, the outputs of the pump and the signal lasers are optically multiplexed to produce a 20-GHz pump-pulse pattern (11111111) and a 20-Gbit/s data-packet pattern (11001100) at the repetition rate of the lasers (14MHz).

In the first experiment, we injected the 5ps 14Mbit/s packet pattern (8 *ones* followed by 24 *zeros*) without using the multiplexer. The stored data packet is monitored at port S with use of a narrow-bandwidth detector having 100-ns response time. Figure 19 shows the loading and the stored data packets at the idler wavelength of 1558nm that are recorded by means of a digital storage scope. The 32-bit data packet is loaded 8 times and then switched off for the next 508

packet durations, until the next loading session. Figure 19(a) shows the envelopes of the data packets on a long time scale, where each packet is only visible as a peak. The higher 8 peaks correspond to the loading packets whereas the lower peak levels are the stored packet for up to 508 circulations (1ms duration) until the next loading event. Note that the envelopes of the stored packet and the background remain uniform between the loading events. Figure 19(b) and (c) show the details of the stored-packet envelopes at different zoomed-in positions. Each big envelope corresponds to the response of the photodetector while being charged by the 8 *one* bits in the packet, whereas the valleys in between correspond to the photodetector being discharged during the following 24 *zero* bits. The 8 small spikes on the rising side of the envelope show the timing positions of the 8 *one* pulses. Note that even after 508 circulations, the stored data packet, Figure 19(c), looks exactly the same as the initial loading packet, Figure 19(b).
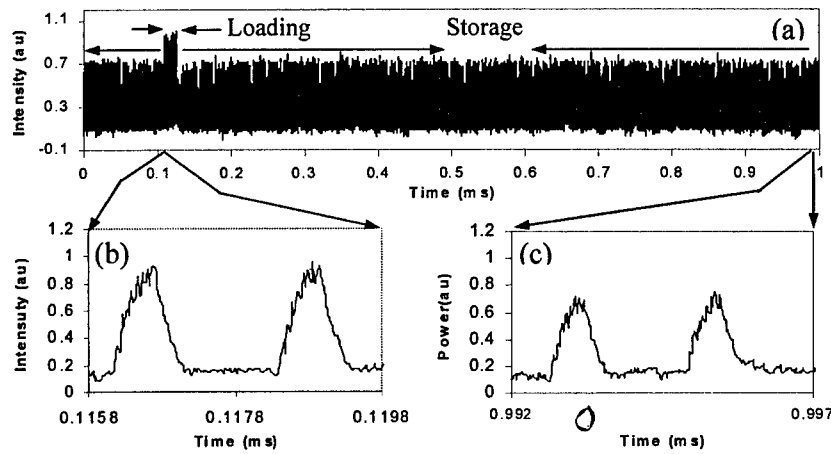
Figure 19 (a) The loading packets and the stored data packets following loading. (b) Close-up view of loading packets. (c) The close-up view after 1ms of storage.
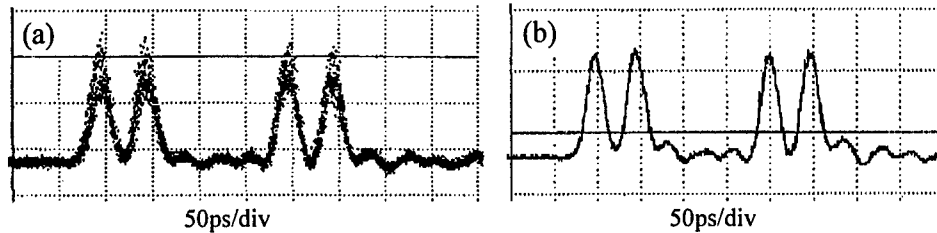
Figure 20 (a) Eye diagram of the loading and stored packets with 1.2s persistence-time setting on the CSA. (b) Single-shot waveform of the data packet after 6s of storage in the buffer.

In Figure 20, we present results of the high-speed experiment. Figure 20(a) shows the eye diagram of the stored 20Gbit/s data packet, as measured by using a 25GHz-bandwidth detector-sampling-scope combination. The relatively high amplitude jitter in the eye diagram is an artifact owing to the periodic loading. The amplitude of the *ones* in the loading packet is higher than that in the stored packet (cf. Figure 19). So, in Figure 20(a), which is a result of 1200 loading/storage sessions during the 1.2s persistence time of the storage scope, the higher levels are the *ones* in the loading packets whereas the lower levels are those in the stored packets. Note that the level

of *zeros* in the stored packets did not build up during the overlap of more-than thousand loading/storage events. Figure 20(b) is the single-shot waveform of the stored data packet after the loading has been completely blocked. The packet stays in the buffer for seconds without any need for adjustment.

In summary, we have employed intracavity all-optical soliton control, for the first time to our knowledge, to achieve buffering of a picosecond-pulse data packet. The technique combines the dynamic parametric-gain modulation provided by a pulsed-pumped NOLM with the soliton shaping property of a NALM. A picosecond-pulse 20Gbit/s-packet pattern is stored for up to seconds. We believe the buffer can be scaled up to much higher speeds by use of high-nonlinearity fibers and high-power EDFAs.

4 References

1. B. H. Hoerman, B. M. Nichols, M. J. Nystrom, and B. W. Wessels, "Dynamic Response of the Electro-optic Effect in Epitaxial $KNbO_3$," Appl. Phys. Lett. **75**, 2707 (1999).

2. D. M. Gill, G. M. Ford, B. A. Block, S.-S. Kim, B. W. Wessels, and S. T. Ho, "Guided Wave Absorption and Fluorescence in Epitaxial $Er:BaTiO_3$ on MgO," Thin Solid Films **356**, 126 (2000).

3. F. Niu, B. H. Hoerman, and B. W. Wessels, "Growth and Microstructure of MgO Thin Films on Si <100> Substrates by Metalorganic Molecular Beam Epitaxy," Appl. Surf. Science **161**, 74–77 (2000).

4. F. Niu, B. H. Hoerman, and B. W. Wessels, "Epitaxial Thin Films of MgO on Si Using Metalorganic Molecular Beam Epitaxy JVST B, **18 (4)** 2146–2150 (2000).

5. G. M. Ford, A. Teren, and B. W. Wessels, "Luminescent Properties of Er-doped $BaTiO_3$ Thin Films for Optical Waveguides," Proc SPIE, **3622** (1999).

6. G-C. Yi, B. A. Block, G. M. Ford, B. W. Wessels, "Luminescence Quenching in Er-doped $BaTiO_3$ Thin Films," Appl. Phys. Lett. **73**, (1998) pp. 1625–27.

7. S. Chattopadhyay, A. Teren, and B. W. Wessels, "Strain in Epitaxial $BaTiO_3$ Thin Films Prepared by MOCVD," MRS Proc., **541** (1999) pp. 101–106.

8. B. H. Hoerman, G. M. Ford, L. D. Kaufman, and B. W. Wessels, "Dielectric Properties of Epitaxial $BaTiO_3$ Thin Films," Appl. Phys. Lett., **73** (1998) pp. 2248–50.

9. Zgonik, M., Bernasconi, P., Duelli, M., Schlesser, R., Gunter, P., Garret, M. H., Rytz, D., Zhu, Y., and Wu, X., "Dielectric, elastic, piezoelectric, electro-optic, and elasto-optic tensors of $BaTiO_3$ crystals," Phys. Rev. B, 1994, **50**, (9), pp. 5941–5949.

10. Wills L. A., Wessels B. W., Richeson D. S., Marks T. J., "Epitaxial growth of BaTiO3 thin films by organometallic chemical vapor," Appl. Phys. Lett., 1992, **60**, (1), pp. 41–43.

11. Private communication with Brent Hoerman. In MOCVD grown $BaTiO_3$ on <100> MgO, c-axis of most of the film is observed aligned with <100> or <010> of MgO.

12. D. Rafizadeh, J. P. Zhang, S. C. Hagness, A. Taflove, R. C. Tiberio, K. A. Stair and S. T. Ho, "Waveguide-coupled AlGaAs/GaAs microcavity ring and disk resonators with high finesse and 21.6-nm free space spectral range, "*Opt. Lett.*, vol. 22, pp. 1244-1246, 1997.

13. S. R. Sakamoto, C. Ozturk, Y. T. Byun, J. Ko, and N. Dagli, "Low-loss substrate-removed (SURE) optical waveguides in GaAs-AlGaAs epitaxial layers embedded in organic polymers," *IEEE Photon. Technol. Lett.*, vol. 10, pp. 985-987, 1998.

14. D. Rafizadeh, J. P. Zhang, R. C. Tiberio, and S. T. Ho, "Propagation loss measurements in semiconductor microcavity ring and disk resonators," *IEEE J. Lightwave Technol.*, vol. 16, pp. 1308-1313, 1998.

15. M. K. Chin, D. Y. Chu, and S. T. Ho, "Estimation of the spontaneous emission factor for microdisk lasers via the approximation of whispering gallery modes", *J. Appl. Phys.*, 75(7), pp. 3302-3307, 1994.

16. Y Ma, S. H. Chang, S. Park, L. Wang, and S. T. Ho, "InGaAsP thin film microdisk resonators fabricated by polymer wafer bonding for wavelength add-drop filters", to be published in *IEEE Photon. Technol. Lett.*

17. Y. Ma, S. Park, L. Wang, and S. T. Ho, "Low-loss and strongly confined InGaAsP/InP optical waveguide fabricated by Benzocyclobutene wafer bonding", *LEOS'99*, paper ThL3, 1999.

18. B. Glance, J. M. Wiesenfeld, U. Koren, A. H. Gnauck, H. M. Presby, and A. Jourdan, Electronics Letters, vol. 28, no. xx, pp. 1714–1716 (1992).

19. T. Durhuus, C. Joergensen, B. Mikkelsen, R. J. S. Pedersen, and K. E. Stubkjaer, IEEE Photon. Technol. Lett. **6**, 53 (1994).

20. S. Murata, A. Tomita, J. Shimizu, and A. Suzuki, IEEE Photon. Technol. Lett. **3**, 1021 (1991).

21. E. Iannone and R. Sabella, J. Lightwave Technol. **13**, 312 (1995).

22. J. K. Lucek and K. Smith, Opt. Lett. **18**, 1226 (1993).

23. G. Raybon, B. Mikkelsen, U. Koren, B. I. Miller, K. Dreyer, L. Boivin, S. Chandrasekhar, and C.A. Burrus, "20 Gbit/s all-optical regeneration and wavelength conversion using SOA based interferometers," in *Optical Fiber Communication Conference*, OSA Technical Digest (OSA, Washington DC, 1999), paper FB2.

24. L. E. Adams, E. S. Kintzer, and J. G. Fujimoto, "Performance and scalability of an all-optical clock recovery figure-eight laser," *IEEE Photonics Technology Letters*, Vol. 8, No. 1, pp. 55-57, 1996.

25. D. K. Serkland and P. Kumar, "Tunable fiber-optic parametric oscillator," *Opt. Lett.*, vol. 24, no. 2, pp. 92–94, Jan. 1999.

26. M. E. Marhic, N. Kagi, T.-K Chiang, and L. G. Kazovsky, "Broadband fiber optical parametric amplifiers," *Opt. Lett.*, vol. 21, no. 8, pp. 573–575, Apr. 1996.

27. Y. Su, L. Wang, A. Agarwal, and P. Kumar, "All-optical limiter using gain flattened fiber parametric amplifier," Electronics Letters, vol. 36, no. 13, 2000, pp. 1103–1105.

28. D. von der Linde, Appl. Phys. B **39**, 201 (1986).

29. S. Spalter, G. Lenz, R. E. Slusher, H. Y. Hwang, J. Zimmerman, T. Katsufuji, S.-W. Cheong, and M. E. Lines, "Highly nonlinear chalcogenide glasses for ultrafast all-optical switching in optical TDM communication systems," in *Optical Fiber Communication Conference*, OSA Technical Digest (OSA, Washington DC, 2000), paper ThI4.

30. G. Lenz, J. Zimmermann, T. Katsufuji, M.E. Lines, H.Y. Hwang, S. Spalter, R.E. Slusher, and S.-W. Cheong, "Large Kerr effect in bulk Se-based chalcogenide glasses," Opt. Lett. **25**, 254 (2000).

31. D. D. Marcenac, D. Nesset, A. E. Kelly, M. Brierley, A. D. Ellis, D. G. Moodie, and C. W. Ford, "40Gb/s transmission over 406km of NDSF using mid-span spectral inversion by four-wave mixing in a 2mm long semiconductor optical amplifier," Electron. Lett. **33** (10), 879–880 (1997).

32. I. Brener, B. Mikkelsen, K. Rottwitt, W. Burkett, G. Raybon, J.B. Stark, K. Parameswaran, M.H. Chou, M.M. Fejer, E.E. Chaban, R. Harel, D.L. Philen, and S. Kosinski, "Cancellation of all Kerr nonlinearities in long fiber spans using a LiNbO$_3$ phase conjugator and Raman amplification," in *Optical Fiber Communication Conference*, OSA Techinical Digest (OSA, Washington DC, 2000), post deadline paper PD33.

33. G. P. Agrawal, *Nonlinear Fiber Optics*, Academic Press, New York, 1995, chap. 7.

34. Y. Su, L. Wang, A. Agarwal, and P. Kumar, "Wavelength-tunable all-optical clock recovery using a fiber-optic parametric oscillator," *Optics Communications*, vol. 184, no. 1–4, 2000, pp. 151–156.

35. L. Wang, Y. Su, A. Agarwal, and P. Kumar, "An all-optical picosecond-pulse packet buffer based on four-wave mixing loading and intracavity soliton control," post-deadline paper presented at the *2000 Conference on Lasers and Electro-Optics* (CLEO'2000) held in San Francisco, California, May 7-12, 2000. See: CLEO'00 Post-deadline Technical Digest (Optical Society of America, Washington, D.C. 2000) paper CPD20.

36. Michael Eiselt, "The impact of non-linear fiber effects on fiber choice for ultimate transmission capacity," *Optical Fiber communication Conference*, OSA Technical Digest (OSA, Washington DC, 2000), TuE1 pp 58-60

37. Jonas Hansryd and Peter A. Andrekson, "Broadband CW pumped fiber optical parametric amplifier with 49 dB gain and wavelength conversion efficiency," *Optical Fiber communication Conference*, OSA Technical Digest (OSA, Washington DC, 2000), PD3-2

38. S. Spalter, G. Lenz, R.E. Slusher, H.Y. Hwang, J. Zimmermann, T. Katsufuji, S-W. Cheong, and M.E. Lines, "Highly nonlinear chalcogenide glasses for ultrafast all optical switching in optical TDM communication systems," *Optical Fiber communication Conference*, OSA Technical Digest (OSA, Washington DC, 2000), ThI4 pp 137-139

39. K. L. Hall and K. A. Rauschenbach, *IEEE Photon. Technol. Lett.*, vol. 10, No.3, pp. 442–444, (1998).

40. J. D. Moores, W. S. Wong, and K. L. Hall, *Opt. Lett.*, vol. 20, No. 24, pp.2547–2549, (1995).

41. A. Agarwal, L. Wang, Y. Su, and P. Kumar, *OFC'2000, Technical Digest*, Tuesday, March 7, pp. 216–218, (2000).

42. A. J. Pousite, K. J. Blow, R. J. Manning, *Opt. Commun.*, vol. 140, pp. 184–186, (1997).

43. L. Wang, Y. Su, A. Agarwal, and P. Kumar, *OFC'2000, Technical Digest*, March 9, pp.235–237, (2000).

44. M. Nakazawa, H. Kubota, E. Yamada, and K. Suzuki, *Electron. Lett.*, vol. 28, no.12, pp. 1099–1100, (1992).

REPORT DOCUMENTATION PAGE

AFRL-SR-AR-TR-05-

O443

1. AGENCY USE ONLY *(Leave blank)*	2. REPORT DATE	3. REPORT TYPE AND DATES COVERED
		01 Jun 1996 - 30 Sep 2001 FINAL

4. TITLE AND SUBTITLE
INTEGRATED DEVICES FOR TERABIT PER SECOND 1.3 AND 1.5 MICRON NETWORK APPLICATIONS

5. FUNDING NUMBERS
61103D
3483/RS

6. AUTHOR(S)
PROFESSOR KUMAR

7. PERFORMING ORGANIZATION NAME(S) AND ADDRESS(ES)
NORTHWESTERN UNIVERSITY
633 CLARK STREET
EVANSTON IL 60208-1110

8. PERFORMING ORGANIZATION REPORT NUMBER

9. SPONSORING/MONITORING AGENCY NAME(S) AND ADDRESS(ES)
AFOSR/NE
4015 WILSON BLVD
SUITE 713
ARLINGTON VA 22203

10. SPONSORING/MONITORING AGENCY REPORT NUMBER
F49620 - 96-1-0262

11. SUPPLEMENTARY NOTES

12a. DISTRIBUTION AVAILABILITY STATEMENT
DISTRIBUTION STATEMENT A: Unlimited

12b. DISTRIBUTION CODE

13. ABSTRACT *(Maximum 200 words)*
As part of the vision of widespread deployment of all-optical network the multidisciplinary university research initiative at Northwestern had the following accomplishments: 1. Developed optically active ferroelectric thin films for waveguides modulators which included: 1.1 The synthesis of epitaxial ferroelectric vapor phase epitaxy (MOVPE); 1.2 Development of thin film ferroelectric electro-optic modulators; 1.3 Development of Er-doped thin film optical amplifier; and 1.4 Integration of epitaxial ferroelectric waveguide structures on silicon using metalorganic molecular beam epitaxy (MOMBE) 2. Realization of Nanoscale Waveguide-Coupled Microcavity Resonators. Improved significantly the characteristics of channel add-drop filters based on the InGaAsP/InP thin film microcavity resonators coupled to nanoscale waveguides. The work was the first demonstration of a working device using InGaAsP/InP system, which is more difficult A1GaAsIGaAs system. 3. Realization of TDM Applications of Fiber-optic Parametric Nonlinearities, which included: 3.1 Wavelength-tunable all-optical clock recovery using a fiber-optic parametric oscillator; 3.2 All-optical limiter using a gain flattened fiber parametric amplifier; 3.3 An all-optical picosecond-pulse packet buffer based on four-wave, mixing loading and intracavity soliton control they employed intracavity all-optical soliton control, for the first time, to achieve buffering of a picosecond-pulse data packet. The technique combines the dynamic parametric-gain modulation provided by a pulsed-pumped NOLM with the soliton shaping property of a NALM. A picosecond-pulse 20Gbit/s-packet pattern is stored for up to seconds.

14. SUBJECT TERMS

15. NUMBER OF PAGES

16. PRICE CODE

17. SECURITY CLASSIFICATION OF REPORT	18. SECURITY CLASSIFICATION OF THIS PAGE	19. SECURITY CLASSIFICATION OF ABSTRACT	20. LIMITATION OF ABSTRACT
Unclassified	Unclassified	Unclassified	UL